Article

Gram-scale bottom-up flash graphene synthesis

https://doi.org/10.1038/s41586-020-1938-0

Received: 28 May 2019

Accepted: 22 October 2019

Published online: 27 January 2020

Duy X. Luong[1,2], Ksenia V. Bets[3], Wala Ali Algozeeb[2], Michael G. Stanford[2], Carter Kittrell[2], Weiyin Chen[2], Rodrigo V. Salvatierra[2], Muqing Ren[2], Emily A. McHugh[2], Paul A. Advincula[2], Zhe Wang[2], Mahesh Bhatt[4], Hua Guo[3], Vladimir Mancevski[2], Rouzbeh Shahsavari[4,5]*, Boris I. Yakobson[2,3,6]* & James M. Tour[2,3,6]*

Most bulk-scale graphene is produced by a top-down approach, exfoliating graphite, which often requires large amounts of solvent with high-energy mixing, shearing, sonication or electrochemical treatment[1–3]. Although chemical oxidation of graphite to graphene oxide promotes exfoliation, it requires harsh oxidants and leaves the graphene with a defective perforated structure after the subsequent reduction step[3,4]. Bottom-up synthesis of high-quality graphene is often restricted to ultrasmall amounts if performed by chemical vapour deposition or advanced synthetic organic methods, or it provides a defect-ridden structure if carried out in bulk solution[4–6]. Here we show that flash Joule heating of inexpensive carbon sources—such as coal, petroleum coke, biochar, carbon black, discarded food, rubber tyres and mixed plastic waste—can afford gram-scale quantities of graphene in less than one second. The product, named flash graphene (FG) after the process used to produce it, shows turbostratic arrangement (that is, little order) between the stacked graphene layers. FG synthesis uses no furnace and no solvents or reactive gases. Yields depend on the carbon content of the source; when using a high-carbon source, such as carbon black, anthracitic coal or calcined coke, yields can range from 80 to 90 per cent with carbon purity greater than 99 per cent. No purification steps are necessary. Raman spectroscopy analysis shows a low-intensity or absent D band for FG, indicating that FG has among the lowest defect concentrations reported so far for graphene, and confirms the turbostratic stacking of FG, which is clearly distinguished from turbostratic graphite. The disordered orientation of FG layers facilitates its rapid exfoliation upon mixing during composite formation. The electric energy cost for FG synthesis is only about 7.2 kilojoules per gram, which could render FG suitable for use in bulk composites of plastic, metals, plywood, concrete and other building materials.

In the flash Joule heating (FJH) process, amorphous conductive carbon powder is lightly compressed inside a quartz or ceramic tube between two electrodes (Fig. 1a, Supplementary Fig. 1). The system can be at atmospheric pressure, or under a mild vacuum (~10 mm Hg) to facilitate outgassing. The electrodes can be copper, graphite or any conductive refractory material, and they fit loosely into the quartz tube to permit outgassing upon FJH. High-voltage electric discharge from a capacitor bank brings the carbon source to temperatures higher than 3,000 K in less than 100 ms, effectively converting the amorphous carbon into turbostratic FG. In high-resolution transmission electron microscopy (HR-TEM) analysis (Fig. 1b, c), the misoriented layers of FG exhibit the expected Moiré patterns, whereas FG derived from spent coffee grounds also shows hexagonal single-layer graphene (Fig. 1d).

High-quality graphene can be quickly identified by Raman spectroscopy[7–10]. FG from carbon black (CB-FG) has an intense 2D peak. As seen in the Raman mapping of CB-FG in Fig. 1e, the intensity of the 2D band relative to the G band ($I_{2D/G}$) is greater than 10 in many locations. The extremely low intensity of the D band indicates the low defect concentration of these FG products, which contributes to the amplification of the 2D band. Thus, the unusually high $I_{2D/G} = 17$ (Fig. 1e) of CB-FG is the highest value reported so far for any form of graphene, and is probably an outcome of the extreme temperature reached in the flash process, which outgasses non-carbon elements from the system. Additionally, the two peaks TS_1 and TS_2 at ~1,886 cm^{-1} and ~2,031 cm^{-1}, respectively, confirm the turbostratic nature of FG (Supplementary Figs. 2, 3), which is discussed extensively in Supplementary Information and Supplementary Table 1[11,12].

The X-ray diffraction (XRD) pattern of FG shows a well defined (002) peak indicating successful graphitization of the amorphous carbon. The (002) peak of FG occurs at diffraction angle $2\theta = 26.1°$,

[1]Applied Physics Program, Rice University, Houston, TX, USA. [2]Department of Chemistry, Rice University, Houston, TX, USA. [3]Department of Materials Science and NanoEngineering, Rice University, Houston, TX, USA. [4]C-Crete Technologies, Stafford, TX, USA. [5]Department of Civil and Environmental Engineering, Rice University, Houston, TX, USA. [6]Smalley-Curl Institute and the NanoCarbon Center, Rice University, Houston, TX, USA. *e-mail: rouzbeh@ccretetech.com; biy@rice.edu; tour@rice.edu

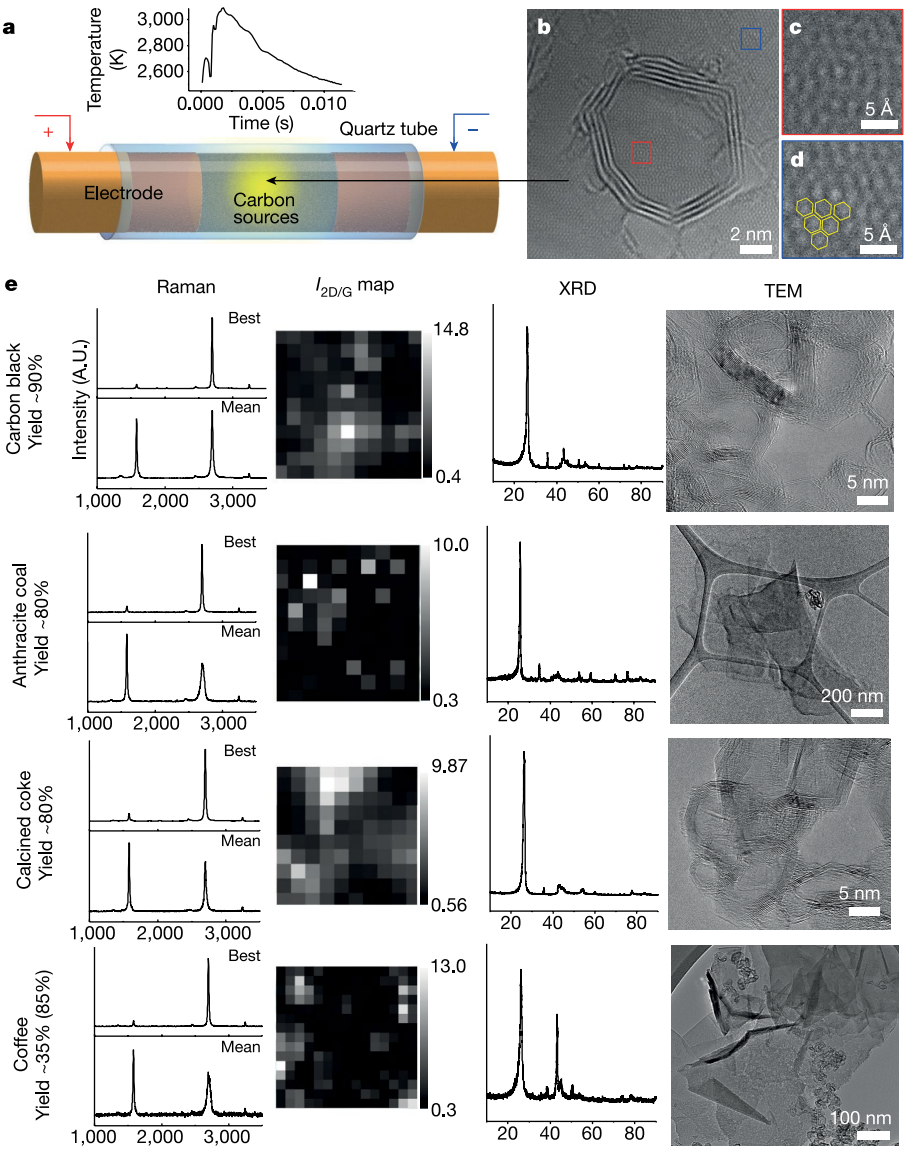

Fig. 1 | FG synthesized from various carbon sources. a, Schematic of the FJH process, and plot of the temperature rise versus time during flashing (inset). **b**–**d**, HR-TEM image of CB-FG on top of a single layer of coffee-derived FG. **e**, Characterization results, including Raman spectra (showing the best and the mean obtained spectra), XRD spectra and TEM images for FG derived from various carbon sources. The coffee-derived FG is made from used coffee grounds; the smaller graphene particles within large graphene sheets come from the carbon black conductive additive. Each pixel in the Raman mapping is 4 μm^2 using a 50× magnification. All Raman samples were prepared from the powdered product after FJH; the samples were not exposed to the solvent before Raman analysis. Coffee is about 40% carbon, so the yield based on the starting carbon content is ~85%. The sample size for the mean Raman spectrum is 10.

which corresponds to an interlayer spacing of I_c = 3.45 Å. This spacing is larger than that in a typical Bernal (AB-stacked) graphite, 3.37 Å, indicating the expanded and turbostratic structure of FG. The (002) peak was found to be unsymmetric, with a tail at small angles, which further suggests the turbostratic nature of FG[13]. The flash process is fast enough to prevent AB stacking. CB-FG has a surface area of ~295 m^2 g^{-1} with pore size <9 nm, as measured by Brunauer–Emmett–Teller analysis (Supplementary Fig. 4). Calcined petroleum coke (CPC) also works well for conversion to CPC-FG (Fig. 1e, Supplementary Table 2) which has a similar nanostructure to that of CB-FG. Together with carbon black, CPC is listed as a non-graphitized carbon source (Supplementary Table 3)[14]. The average size of CB-FG and CPC-FG is ~13 nm and ~17 nm, respectively (Supplementary Figs. 5, 6). The yield of the FJH process is as high as 80% to 90% from high-carbon sources such as carbon black, calcine coke or anthracite coal, and the electric energy needed for their conversion is ~7.2 kJ g^{-1} (Supplementary Information).

In the case of coffee grounds, the used grounds were mixed with 5 wt% carbon black to increase its conductivity—alternatively, we could use 2–5 wt% FG from a previous run as the conductive additive. Coffee grounds, being predominantly carbohydrate, are ~40% carbon. Hence, the yield of graphene of ~35% (Fig. 1e) would be ~85% conversion of the coffee carbon content into graphene, whereas the heteroatoms sublime out at these reaction temperatures (>3,000 K). Anthracite can be sufficiently conductive to be used in the FJH reactor, but better results were obtained by adding 5 wt% carbon black. Although a black FG powder is produced regardless of the starting material, FG from graphitizing carbons—such as from used coffee grounds (C-FG) and anthracite coal (A-FG) (see Supplementary Information for definitions of graphitizing and non-graphitizing carbons; see also Supplementary Table 3)—has

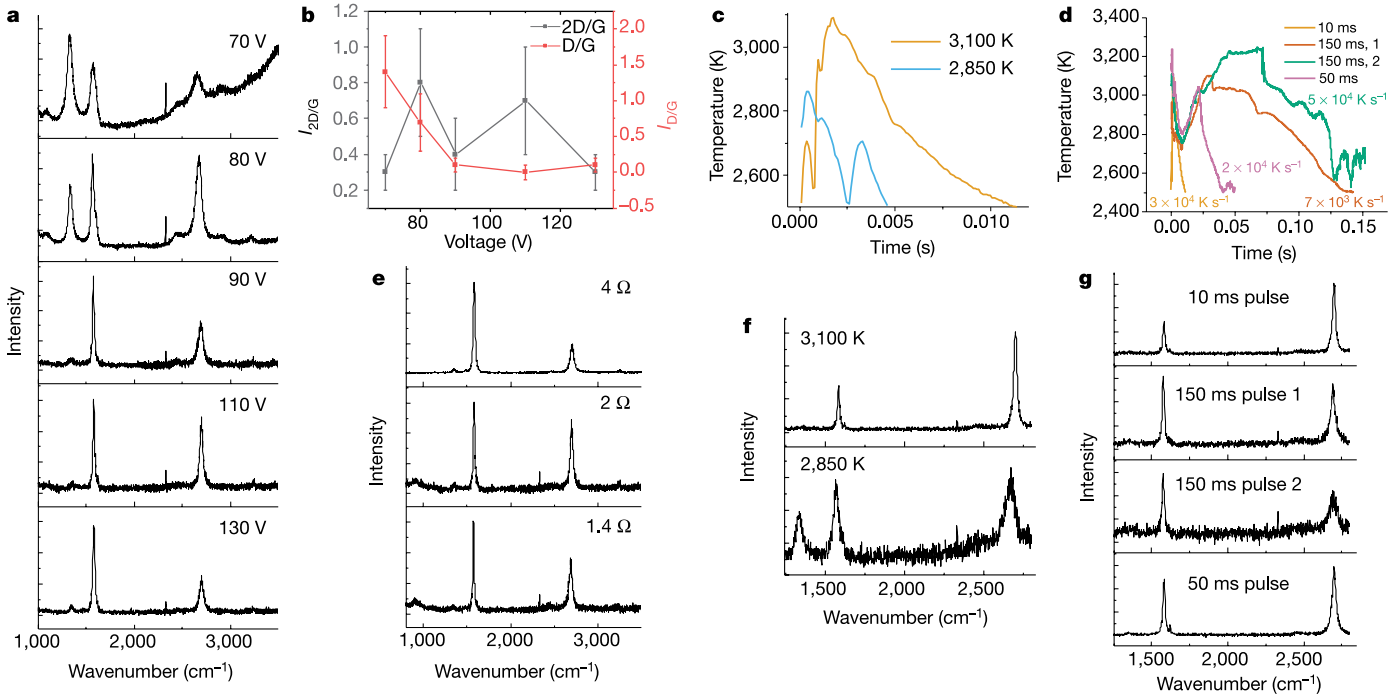

Fig. 2 | FJH critical parameters. a, Raman spectra of CB-FG with increasing flashing voltage (top to bottom). **b**, $I_{2D/G}$ and $I_{D/G}$ ratios of CB-FG at different flashing voltages. The bars represent 1 s.d. ($n = 10$). **c**, Time–temperature graph of CB-FG reacted at different temperatures. The temperature is regulated by the flashing voltage. **d**, Time–temperature graph of CB-FG reacted at different flashing durations. The flashing duration is regulated by the sample compression between the electrodes, which affects the sample conductivity. The numbers within the plot represent cooling rates. **e**, Raman spectra of CB-FG at different compression ratios. Higher compression provides lower resistance to the sample. **f**, Raman spectra of the CB-FG samples shown in **c**. **g**, Raman spectra of the CB-FG samples shown in **d**. The 150-ms pulses 1 and 2 have similar duration but different cooling rates, as shown in **d**. All Raman spectra in the figure were taken at low magnification (5×) to obtain a mean spectrum of the sample from 10 spectra.

different morphologies from CB-FG. Graphitizing carbons produce larger graphene sheets (Supplementary Fig. 7). XRD analysis of C-FG shows, in addition to the dominant (002) peak at 26.0°, a sharp (100) peak at $2\theta = 42.5°$, which is associated with the in-plane interatomic spacing (Fig. 1e). The narrow full width at half-maximum of the (100) peak suggests larger in-plane sheet sizes relative to FG formed from some of the other starting materials. HR-TEM reveals folded graphene sheets in A-FG and C-FG (Fig. 1e) with an average size of 0.5 µm and 1.2 µm (Supplementary Fig. 7), respectively, similar to the size of graphene sheet obtained by exfoliation of graphite[3,15,16]. Selected-area electron diffraction measurements on these samples show both monolayer and turbostratic graphene (Supplementary Figs. 8–10).

Other carbons that are abundant, renewable or waste-sourced can be used, such as charcoal, biochar, humic acid, keratin (human hair), lignin, sucrose, starch, pine bark, olive oil soot, cabbage, coconut, pistachio shells, potato skins, rubber tyres and mixed plastic (Supplementary Fig. 11, Supplementary Table 4), including polyethylene terephthalate (PET or PETE), high- or low-density polyethylene, polyvinyl chloride, polypropylene and polyacrylonitrile. When converting synthetic polymers into FG, the non-carbon atoms sublime out as small molecules, leading to a very-high-carbon-content product, as shown here. However, polymer and rubber depolymerization can also ensue to afford oligomers that sublime before conversion; therefore, it is more economical to use a pyrolysis product where the volatiles are first industrially removed for fuel sources[17] and the residual carbon is converted into FG. This was demonstrated here with rubber-tyre-derived carbon black (Supplementary Fig. 11,Supplementary Tables 2, 4). None of these FG processes was optimized. Optimization was performed only on CB-FG, as described below. The FJH process can provide a facile route to convert these waste products into FG, a potential high-value building-composite additive[18–21].

The graphene $I_{2D/G}$ is optimized by adjusting the sample compression between the electrodes (which affects sample conductivity), the capacitor voltage and the switching duration to control the temperature and duration of the flash (Fig. 2a–g). Increasing the voltage will increase the temperature of the process. The temperature is estimated by fitting the black-body radiation spectrum in the 600–1,100 nm emission (Supplementary Fig. 12). We investigated the quality of CB-FG using Raman spectroscopy at low magnification (see Methods) by varying the time and temperature in the FG synthesis process. At <90 V and <3,000 K, FG has a high D peak, indicating a defective structure (Fig. 2a–c, f). By increasing the voltage output, CB-FG is formed at 3,100 K, which has a low number of defects and almost no D band in the Raman spectrum. Therefore, 3,000 K is a critical temperature for producing higher-quality graphene with a larger $I_{2D/G}$ value.

By increasing the compression on the sample between the two electrodes, the conductivity of the carbon source increases, thus decreasing the discharge time (Fig. 2d, e, g). While maintaining the flash temperature between experimental runs at ~3,100 K, a short flash duration of 10 ms results in a higher 2D band, whereas a flash of 50–150 ms results in a lower 2D band product (Fig. 2g). This indicates that, given more time, the graphene flakes stack, orient and form more layers, lowering the 2D band of the resulting FG. A low cooling rate increases the flash duration and decreases the 2D band[22]. Therefore, to obtain a high $I_{2D/G}$, a thin quartz tube is chosen to accelerate the radiative cooling rate. Interestingly, although the internal temperatures exceed 3,000 K, the external walls of the quartz tubes are only warm to the touch (<60 °C) after the flash process. Most of the heat exits as black-body radiation.

X-ray photoelectron spectroscopy analysis shows a considerable reduction of elements other than carbon in FG and increases in the sp^2 carbon bond content (Supplementary Figs. 13, 14). Carbon has a

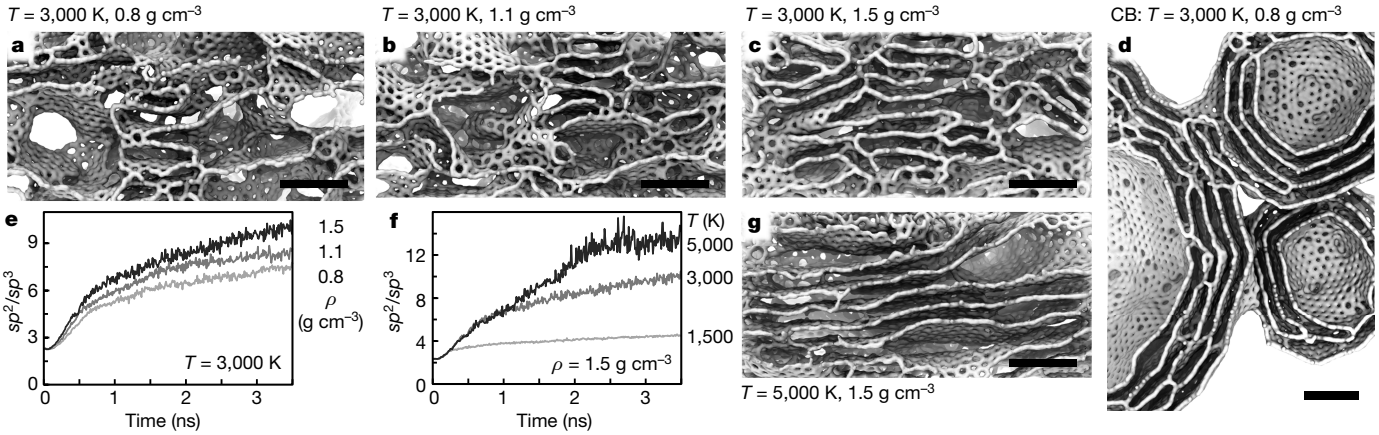

Fig. 3 | Molecular dynamics simulations. Structures with various characteristics (such as micro-porosity, misalignment and size of graphitic domains) kept at a given temperature range (1,500 to 5,000 K) for up to 5×10^{-9} s with a Nosé–Hoover thermostat. **a**–**c**, Sample structures for carbon materials of density 0.8 g cm^{-3} (**a**; sponge-like structure), 1.1 g cm^{-3} (**b**), and 1.5 g cm^{-3} (**c**; high degree of graphitization) after annealing at 3,000 K. **d**, Carbon black with density 0.8 g cm^{-3} and large macro-porosity, after prolonged (5×10^{-9} s) annealing at 3,600 K; polygonal fringes are apparent. **e**–**f**, Change of the structural composition of materials during annealing for materials of different densities ρ (**e**) and for annealing at different temperatures T (**f**). **g**, Structure of material with density 1.5 g cm^{-3} after annealing at 5,000 K; the initial structure is the same as that shown in **c**. All scale bars are 1.5 nm.

high sublimation temperature of ~3,900 K; other elements such as aluminium or silicon volatilize out at <3,000 K.

Thermogravimetric analysis in air shows that FG products are more oxidatively stable than the materials from which they are derived (Supplementary Fig. 15) and more stable than reduced graphene oxide obtained with Hummer's method[23]. In some cases, silicon oxide residues are detected, which come from worn out quartz tubes after multiples uses.

Previous studies have shown that graphene can be synthesized without catalysts at extremely high temperatures[24–26]. However, when FG is optimized as shown here, it can have exceptionally high quality when the reaction time and temperature are controlled. Furthermore, the electric current can facilitate the crystallization of graphene[27]. Degassing of hydrogen, nitrogen and oxygen during the FJH process might contribute to the formation of large and thin graphene sheets in coffee-derived FG because it could prevent stacking of graphene layers, thereby permitting further growth[25,28,29].

To assess the mechanism of the rapid FG growth, we employ large-scale simulations with the AIREBO[30,31] interatomic potential as implemented in the LAMMPS package (see Methods)[32]. Some of the acquired structures are shown in Fig. 3a–d. The low-density materials yield a sponge-like structure (Fig. 3a) during annealing, whereas increased density leads to a high level of graphitization (Fig. 3c). We note the high level of graphitization in the low-density CB sample, where the substantially increased local density is combined with high macro-porosity (Fig. 3d). Additionally, the annealing process is quantified by the sp^2/sp^3 ratio during simulation (Fig. 3e, f). We find that the graphene formation process is strongly impaired at lower temperatures (<2,000 K) but greatly accelerated at higher temperature (5,000 K) (Fig. 3g)—a trend that is also suggested by experiments (Fig. 2f). In the case of carbon black, continuous defect healing during FJH results in the gradual conversion of initially roughly spherical centroid particles into polyhedral shapes (Fig. 3d) that appear as fringes at clearly defined angles in TEM images (see Fig. 1b, e), further confirming the low-defect nature of the produced materials.

The FJH process was scaled up by increasing the quartz tube size. With quartz tubes of 4 mm, 8 mm and 15 mm diameter, 30 mg, 120 mg and 1 g of FG can be synthesized per batch, respectively. Figure 4a shows the amount of CB-FG obtained with the three tube sizes. The shorter flash from the smaller tube results in FG with a higher $I_{2D/G}$. To increase the batch size while maintaining FG quality, flat tubes are helpful because they enable a higher cooling rate (Fig. 4a). For industrial production, we envision that the process can be automated for continuous FG synthesis (Supplementary Fig. 16).

FG was found to be dispersible in water/surfactant (Pluronic F-127) to give highly concentrated dispersions reaching 4 g l^{-1} (Fig. 4b, Supplementary Fig. 17). Using organic solvents, FG has a high degree of dispersibility (Fig. 4c)[33–35], which can be attributed to the turbostratic arrangement permitting efficient exfoliation; the interlayer attraction forces are much lower than in conventionally arranged AB-stacked graphene obtained by graphite exfoliation.

FG composites were explored, revealing considerably enhanced physical properties at small FG loadings. CB-FG–cement composites with 0.05% FG and cured for 28 days had ~25% higher compressive strength than the FG-free control sample (Supplementary Fig. 18). This enhancement in the compressive strength is three times higher than the values reported recently for cement composites reinforced by electrochemically exfoliated graphene with the same graphene loading, and slightly larger than those of other cement–graphene composites[36,37]. The seven-day compressive and tensile strength of CB-FG–cement composites with 0.1% FG loading are ~35% and ~19% higher, respectively, than those of the FG-free control sample (Fig. 4d). These enhancements are almost three times larger than those of other reported graphene–cement composites with the same loading, demonstrating rapid strength development. Scanning electron microscopy images of CB-FG–cement composites (Supplementary Fig. 19) show a homogeneous distribution of FG in the cement matrix. The largely enhanced properties and rapid strength development of CB-FG–cement composites is again attributed to the high dispersibility of the turbostratic CB-FG, which results in greater homogeneity and robust composites (see Supplementary Information for further explanations).

In addition, CB-FG effectively enhances polymer properties. A 0.1 wt% CB-FG–polydimethylsiloxane (PDMS) composite showed ~250% increase in compressive strength compared with PDMS without graphene (Supplementary Fig. 20).

To demonstrate its applicability in electrochemical energy storage devices, C-FG and CPC- FG were also used as electrode materials in a Li-ion capacitor and a Li-ion battery (Supplementary Fig. 21), demonstrating the potential to use FG in advanced energy applications.

In summary, a low-energy bottom-up synthesis of easily exfoliated turbostratic graphene was demonstrated from ultralow-cost carbon sources (such as coal and petroleum coke), renewable resources (such as biochar and rubber tyres) and mixed-waste products (including plastic bottles

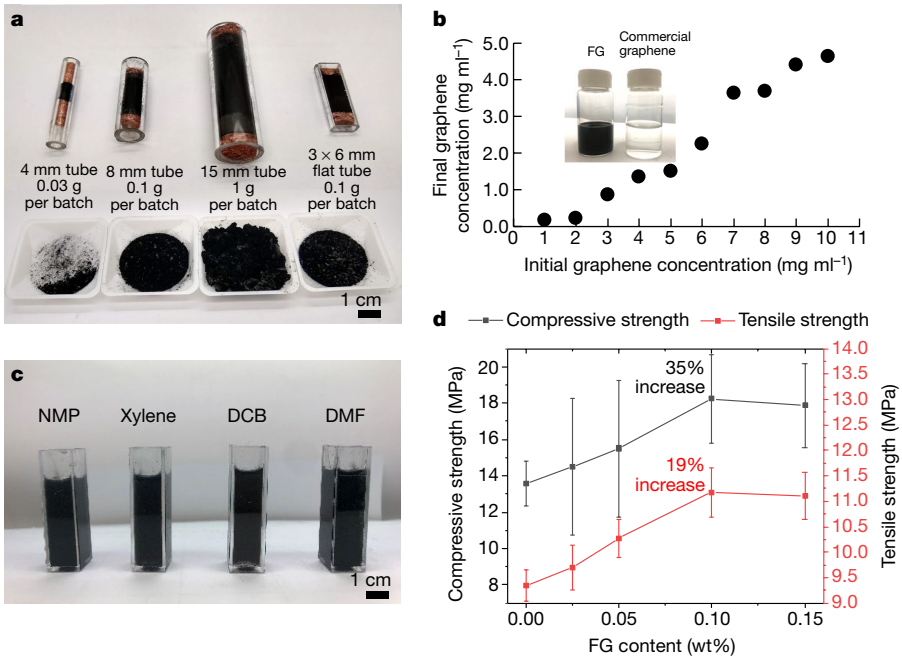

Fig. 4 | Scaling up and applications of CB-FG. a, FJH quartz tubes of different sizes and shapes, used to synthesize FG. Two separate synthesis processes were conducted with each tube, providing the samples in the tube and those in the plastic dishes. **b**, FG dispersion in a water–Pluronic (F-127) solution (1%). The photograph shows the supernatants of 4 g l^{-1} of CB-FG and of 10 g l^{-1} of a commercial sample after centrifugation. The commercial graphene was not stable as a colloid at this concentration, resulting in a clear liquid in the supernatant after centrifugation. **c**, FG dispersion in various organic solvents at 5 g l^{-1}. **d**, Mechanical performance of cement compounded with FG. The error bars represent one standard error ($n = 3$).

and discarded food). Scaling up of the FG synthesis process could provide turbostratic graphene for bulk construction composite materials.

Online content

Any methods, additional references, Nature Research reporting summaries, source data, extended data, supplementary information, acknowledgements, peer review information; details of author contributions and competing interests; and statements of data and code availability are available at https://doi.org/10.1038/s41586-020-1938-0.

1. Allen, M. J., Tung, V. C. & Kaner, R. B. Honeycomb carbon: a review of graphene. *Chem. Rev.* **110**, 132–145 (2010).
2. Yi, M. & Shen, Z. A review on mechanical exfoliation for the scalable production of graphene. *J. Mater. Chem. A* **3**, 11700–11715 (2015).
3. Hernandez, Y. et al. High-yield production of graphene by liquid-phase exfoliation of graphite. *Nat. Nanotechnol.* **3**, 563–568 (2008).
4. Eda, G., Fanchini, G. & Chhowalla, M. Large-area ultrathin films of reduced graphene oxide as a transparent and flexible electronic material. *Nat. Nanotechnol.* **3**, 270–274 (2008).
5. Li, D. et al. Processable aqueous dispersions of graphene nanosheets. *Nat. Nanotechnol.* **3**, 101–105 (2008).
6. Lin, L., Peng, H. & Liu, Z. Synthesis challenges for graphene industry. *Nat. Mater.* **18**, 520–524 (2019).
7. Ferrari, A. C. et al. Raman spectrum of graphene and graphene layers. *Phys. Rev. Lett.* **97**, 187401 (2006).
8. Ferrari, A. C. Raman spectroscopy of graphene and graphite: disorder, electron–phonon coupling, doping and nonadiabatic effects. *Solid State Commun.* **143**, 47–57 (2007).
9. Malard, L. M., Pimenta, M. A., Dresselhaus, G. & Dresselhaus, M. S. Raman spectroscopy in graphene. *Phys. Rep.* **473**, 51–87 (2009).
10. Ni, Z. H. et al. Probing charged impurities in suspended graphene using Raman spectroscopy. *ACS Nano* **3**, 569–574 (2009).
11. Garlow, J. A. et al. Large-area growth of turbostratic graphene on Ni (111) via physical vapor deposition. *Sci. Rep.* **6**, 19804 (2016).
12. Niilisk, A. et al. Raman characterization of stacking in multi-layer graphene grown on Ni. *Carbon* **98**, 658–665 (2016).
13. Li, Z. Q. et al. X-ray diffraction patterns of graphite and turbostratic carbon. *Carbon* **45**, 1686–1695 (2007).
14. Franklin, R. E. Crystallite growth in graphitizing and non-graphitizing carbons. *Proc. R. Soc. Lond.* **209**, 196–218 (1951).
15. Stankovich, S. et al. Synthesis of graphene-based nanosheets via chemical reduction of exfoliated graphite oxide. *Carbon* **45**, 1558–1565 (2007).
16. Cai, M., Thorpe, D., Adamson, D. H. & Schniepp, H. C. Methods of graphite exfoliation. *J. Mater. Chem.* **22**, 24992–25002 (2012).
17. Miandad, R. et al. Catalytic pyrolysis of plastic waste: moving toward pyrolysis based biorefineries. *Front. Energy Res.* **7**, 27 (2019).
18. Gibb, B. C. Plastics are forever. *Nat. Chem.* **11**, 394–395 (2019).
19. Parfitt, J., Barthel, M. & Macnaughton, S. Food waste within food supply chains: quantification and potential for change to 2050. *Philos. Trans. R. Soc. B* **365**, 3065–3081 (2010).
20. Gustavsson, J., Cederberg, C., Sonesson, U., van Otterdijk, R. & Meybeck, A. *Global Food Losses and Food Waste: Extent, Causes and Prevention* (FAO, 2011); http://www.fao.org/3/a-i2697e.pdf.
21. Jambeck, J. R. et al. Plastic waste inputs from land into the ocean. *Science* **347**, 768–771 (2015).
22. Yao, Y. et al. Carbothermal shock synthesis of high-entropy-alloy nanoparticles. *Science* **359**, 1489–1494 (2018).
23. Advincula, P. A. et al. Accommodating volume change and imparting thermal conductivity by encapsulation of phase change materials in carbon nanoparticles. *J. Mater. Chem. A* **6**, 2461–2467 (2018).
24. Chakrabarti, A. et al. Conversion of carbon dioxide to few-layer graphene. *J. Mater. Chem.* **21**, 9491–9493 (2011).
25. Lin, J. et al. Laser-induced porous graphene films from commercial polymers. *Nat. Commun.* **5**, 5714 (2014).
26. Nepal, A., Singh, G. P., Flanders, B. N. & Sorensen, C. M. One-step synthesis of graphene via catalyst-free gas-phase hydrocarbon detonation. *Nanotechnology* **24**, 245602 (2013).
27. Huang, J. Y. et al. Real-time observation of tubule formation from amorphous carbon nanowires under high-bias Joule heating. *Nano Lett.* **6**, 1699–1705 (2006).
28. Harris, P. J. F. Engineering carbon materials with electricity. *Carbon* **122**, 504–513 (2017).
29. Luong, D. X. et al. Laser-induced graphene fibers. *Carbon* **126** 472–479 (2017).
30. Stuart, S. J., Tutein, A. B. & Harrison, J. A. A reactive potential for hydrocarbons with intermolecular interactions. *J. Chem. Phys.* **112**, 6472–6486 (2000).
31. Brenner, D. W. et al. A second-generation reactive empirical bond order (REBO) potential energy expression for hydrocarbons. *J. Phys. Condens. Matter* **14**, 783–802 (2002).
32. Plimpton, S. Fast parallel algorithms for short-range molecular dynamics. *J. Comput. Phys.* **117**, 1–19 (1995).
33. Xu, Y. et al. Liquid-phase exfoliation of graphene: an overview on exfoliation media, techniques, and challenges. *Nanomaterials* **8**, 942 (2018).
34. O'Neill, A., Khan, U., Nirmalraj, P. N., Boland, J. & Coleman, J. N. Graphene dispersion and exfoliation in low boiling point solvents. *J. Phys. Chem. C* **115**, 5422–5428 (2011).
35. Dong, L. et al. A non-dispersion strategy for large-scale production of ultra-high concentration graphene slurries in water. *Nat. Commun.* **9**, 76 (2018).
36. Liu, J., Li, Q. & Xu, S. Reinforcing mechanism of graphene and graphene oxide sheets on cement-based materials. *J. Mater. Civ. Eng.* **31**, 04019014 (2019).
37. Krystek, M. et al. High-performance graphene-based cementitious composites. *Adv. Sci.* **6**, 1801195 (2019).

Methods

FJH system

The FJH set up is detailed in Supplementary Fig. 1. Inside a quartz tube, two loosely fitting electrodes compress the carbon source using two copper-wool plugs or graphite spacers to contact the carbon sources to allow degassing of volatile materials. The compressing force is controllable by a modified small vice so as to minimize the sample resistance to 1–1,000 Ω, and is key to obtaining a good flash reaction (0.004–4 S cm^{-1}). To control the discharge time, a mechanical relay with programmable millisecond-level delay time is used. The entire sample reaction chamber is placed inside a low-pressure container (plastic vacuum desiccator) for safety and to facilitate degassing. However, the FJH process works equally well at 1 atm. The capacitor bank consists of 20 capacitors with a total capacitance of 0.22 F. Each capacitor is connected to the main power cable (or bus) by a circuit breaker that is also used as a switch to enable/disable each capacitor. The capacitor bank is charged by a d.c. supply capable of reaching 400 V. The first prototype system is placed conveniently on one plastic mobile cart (Supplementary Fig. 1b). Using a large 15-mm-diameter quartz tube, we achieve synthesis of 1 g of FG per batch using the FJH process.

Safety notice: the capacitor bank is capable of generating fatal electric pulses. Therefore, the following steps are taken to protect the operator as well as the circuit, and we strongly suggest that these measures be followed. Details of the circuit can be found in Supplementary Fig. 1a. Darkened safety glasses should be worn to protect eyes from the bright light during the discharge flashing process.

The voltage and current ratings for the circuit breaker are appropriate for the maximum voltage and the anticipated maximum current that will be supplied by each capacitor to the FJH discharge on the basis of a discharge time of 50–200 ms. We use the maximum charging and bleeding voltages at ~400 V with maximum currents of 0.7 A and 0.1 A, respectively. The pulse discharging voltage to the sample is ~400 V and current can reach up to 1,000 A in <100 ms. A 24-mH inductor is used to avoid current spikes while using the mechanical relay. Without the inductor, the mechanical relay could be prone to high-current arcing during the intermittent closing of the circuit. To protect the inductor from the spike voltage when shutting off the current, a diode and a low-resistance resistor with appropriate ratings are connected parallel to the inductor. Additionally, to protect the capacitor from reverse polarity in case of oscillatory decay (which can occur in a fast discharge), an appropriate diode is placed parallel to the capacitor bank.

Characterization

The resultant FG products were characterized by scanning electron microscopy (SEM) using an FEI Helios NanoLab 660 DualBeam SEM system at 5 kV with a working distance of 10 mm. X-ray photoelectron spectroscopy (XPS) data were collected with a PHI Quantera SXM Scanning X-ray Microprobe with a base pressure of 5×10^{-9} torr. Survey spectra were recorded using 0.5-eV steps with a pass energy of 140 eV. Elemental spectra were recorded using 0.1-eV steps with a pass energy of 26 eV. All of the XPS spectra were corrected using the C 1*s* peak (284.5 eV) as reference.

TEM images were taken with a JEOL 2100F field-emission gun TEM at 200 kV. Atomic-resolution HR-TEM images were taken with an FEI Titan Themis S/TEM system at 80 keV. Samples were prepared by dropping diluted dispersions (~1 mg ml^{-1} in isopropanol) of the graphene sample (<200 µl) on the TEM Cu grids. The dispersion was prepared using a bath sonicator (~15 min). Electron diffraction was calibrated by a diffraction standard (evaporated Al grid; Ted Pella).

All Raman spectra were collected with as-prepared FG samples atop a glass slide, before exposure to solvent, using a Renishaw Raman microscope and a 532-nm laser with a power of 5 mW. A 50× lens was used for the local Raman spectra in Fig. 1 and a 5× lens for the mean Raman spectra in Fig. 2.

Atomistic modelling

Atomistic simulations were carried out using periodic boundary conditions with ~15,000 atoms per unit cell for all structures except the carbon black model, which contained ~55,000 atoms. The initial configurations were created by random positioning and misorientation of small graphitic flakes of arbitrary shape and up to 8–12 Å in diameter, and subsequently adding randomly positioned individual carbon atoms (the atomic carbon content was ~50% to represent a non-graphitized portion of the source material). Carbon black centroid particles were created by arranging randomly oriented graphitic flakes in roughly spherical shapes with hollow cores and diameters of up to 12 nm, and adding atomic carbon (~50%). The initial configurations were subjected to preliminary annealing at 400 K for 2×10^{-9} s to eliminate irregularities caused by the structure creation protocol, then heated to the target annealing temperature with a heating speed of 0.5×10^{-12} K s^{-1} using a Nose–Hoover thermostat (canonical NVT ensemble) with a temperature damping parameter of 0.025×10^{-12} s. The structures were held at the target annealing temperatures for 5×10^{-9} s (15×10^{-9} s for carbon black).

Preparation of flash graphene dispersion in water–Pluronic solution

FG was dispersed in water–Pluronic (F-127) solution (1%) at concentrations of 1–10 g l^{-1}. The mixture was sonicated in an ultrasonic bath for 40 min to obtain a dark dispersion. The dispersion was subjected to centrifugation at 1,500 rpm (470 relative centrifugal force) for 30 min to remove aggregates using a Beckman Coulter Allegra X-12 centrifuge equipped with a 19-cm-radius rotor. The supernatant was analysed via ultraviolet–visible spectroscopy (Shimadzu). The dispersions were diluted 500 times and the absorbance was recorded at 660 nm. An extinction coefficient of α_{660} = 6,600 l g^{-1} m^{-1} was used to calculate the concentration of graphene in the solution.

Cement sample preparation

FG at various concentrations was dispersed in 1% water–Pluronic (F-127) solution. The dispersion was agitated for 15 min at 5,000 rpm using a shear mixer (Silverson L5MA). The graphene suspension in water was mixed with Portland cement with a water-to-cement ratio of 0.40. The slurry was cast in 5 × 5 × 5 cm^3 cubic polytetrafluoroethylene moulds (for compressive strength measurements) and in 2.5 cm × 3.8 cm cylindrical moulds (for tensile strength measurements). All cubes and cylinders were taken out the moulds after 24 h and placed in water for curing for another 24 h. The compressive and tensile mechanical strengths were measured after 7 and 28 days. For each FG–cement ratio, three samples were cast and tested.

Cement and PDMS testing procedures

Compressive strength. The compression strength tests were performed using a Forney Variable Frequency Drive automatic machine with dual load cells for maximum accuracy.

Tensile strength. Owing to the brittle nature of cement-based materials, the tensile strength was calculated via a splitting test because it gives the most accurate measurement. Special jigs held the cylinders so that the uniaxial compressive force applied to the centre lines of the bottom and top surfaces of the samples caused tensile stress between the points of contact.

Data availability

The datasets generated and/or analysed during the current study are available from the corresponding author on reasonable request.

Acknowledgements We thank G. A. Lopez Silva for preparing the schematic of the FJH process, J. Li for preparing the olive oil soot, Oxbow Calcining International LLC for donating the calcined coke, Ergon Asphalt and Emulsions, Inc. for donating the rubber-tyre-derived carbon black, and Neroval LLC for donating the biochar. K.V.B. and B.I.Y. thank the National Science Foundation (NSF) for support (CBET-1605848) and B. Sastri of the US Department of Energy for discussions. R.S. thanks the partial support of NSF-DMR 1709051. J.M.T. thanks the US Air Force Office of Scientific Research (FA9550-19-1-0296) for support.

Author contributions D.X.L. discovered the FJH conversion of carbon materials to graphene, designed and built the FJH apparatus, designed and built the spectrometer for temperature determination, acquired most of the data, and wrote most of the manuscript. K.V.B. conducted the mechanistic theory calculations under the guidance of B.I.Y. W.A.A. and P.A.A. fabricated some FG samples, and blended and tested the polymer blends. M.G.S. obtained the SEM images and wrote parts of Supplementary Information, especially regarding FG morphology. C.K. assisted with the design of the FG apparatus and the spectrometer, and wrote parts of Supplementary Information regarding turbostratic graphene. R.V.S. obtained most of the TEM images and all of the selected-area electron diffraction data. W.C. and H.G. obtained some of the TEM images. M.R. built and tested the lithium-ion capacitor. C.K. and V.M. assisted D.X.L. in the design and safety features of the FJH system. E.A.M. performed the thermogravimetric analysis. Z.W. obtained the surface area. M.B. obtained the cement and polymer composite data under the guidance of R.S. All aspects of the research were overseen by J.M.T., who co-wrote some sections of the manuscript.

Competing interests The FG synthesis process is the intellectual property of Rice University. J.M.T., D.X.L. and V.M. will be stockholders in Universal Matter Ltd, a company licensing the FG intellectual property of Rice University and scaling up this process. At the time of the writing and submission of this manuscript, the license to Universal Matter has not been consummated. C-Crete Technologies owns intellectual property on the strengthening of graphene–cement/concrete composites. V.M. is now employed by Universal Matter. D.X.L. and J.M.T. will remain full time with Rice University, whereas D.X.L. might be employed by Universal Matter in two years. All conflicts of interest for J.M.T. and D.X.L. are managed through regular disclosure to the Rice University Office of Sponsored Programs and Research Compliance.

Additional information

Supplementary information is available for this paper at https://doi.org/10.1038/s41586-020-1938-0.

Correspondence and requests for materials should be addressed to R.S., B.I.Y. or J.M.T.

Peer review information *Nature* thanks Loh Kian Ping and the other, anonymous, reviewer(s) for their contribution to the peer review of this work.